Controlling Preferential Growth of Chromium – Nitrogen R-HiPIMS and R-DCMS Films by Substrate Magnetic Biasing

S. Vargas, D.S. Galeano-Osorio, *C.E. Castano

Department of Mechanical and Nuclear Engineering, Virginia Commonwealth University, Richmond, VA 23284, USA

* Corresponding Author: cecastanolond@vcu.edu (C.E. Castano)

Abstract

The effect of magnetic biasing on the structure of Cr-N coatings deposited on silicon substrates by reactive magnetron sputtering has been investigated. The magnetic biasing setup consisted of a permanent magnet placed close to the substrate holder to modify the plasma species dynamics and deposition flux. Three magnetic field configurations for reactive direct current magnetron sputtering (R-DCMS) and reactive High Power Impulse Magnetron Sputtering (R-HiPIMS) were compared. Deposition parameters such as deposition time, gun power, substrate distance, temperature, gas pressure, and gas composition were constant through the six R-DCMS/HiPIMS-magnetic-field combinations. Processes were monitored through optical emission spectroscopy (OES) and closely compared to the voltage and current curves at the target/substrate. An excitation mechanism was proposed accounting for the enhanced ionization detected by OES and the implications in the film's growth. The films' stoichiometry, structure, thickness, morphology, and crystal texture were characterized and associated with the process parameters. The R-DCMS processes led to Cr-N solid solution films, while the enhanced reactivity of R-HiPIMS plasma species increased the N content and formed CrN. Overall, the R-DCMS deposited samples were thicker than the R-HiPIMS deposited samples, but the different magnetic field biasing setups allowed for specific control of films' thickness, texture, and microstructure.

1. Introduction

The ability to control the surface of materials lies at the heart of cutting-edge materials research. Various techniques can be pursued to deposit thin films and nanostructures, and in the gas phase, sputtering techniques have found widespread use in many industrial sectors because of their coating uniformity [1–4]. Sputtering techniques have had several variations over the last 50 years. The most straightforward configuration is perhaps the direct current (DC) sputtering, where an electric field accelerates ions from the glow discharge plasma, usually Ar ions, to sputter atoms from the cathode (target material). This basic technique was improved by adding magnets behind the cathode target, which was coined as magnetron sputtering discharge. This implementation adds a crosswise magnetic field over the cathode, increasing the path length of electrons, decreasing scattering, and increasing ionization and deposition rates [4–6]. When a magnetron sputtering discharge is driven by dc voltage or current, it is called a dc magnetron sputtering (DCMS) discharge. More recently, improvements were obtained by using pulsed power magnetron sputtering processes. In this case, low to mid-frequency pulses in the tens to some thousand Hz helped stabilize the arcs during sputtering [2–4,7,8]. This advance allowed defect-free coatings of metals and oxides. This modification also allowed to impose much higher peak power on the targets, changing the dynamics of the process. This latter option is called High Power Impulse Magnetron Sputtering (HiPIMS or sometimes HPPMS), and it has benefits when processing complex-shaped substrates making it an attractive alternative for new research areas. The HiPIMS techniques operate at the same pressure regimes as DC magnetron sputtering, but they were also initially designed to provide enhanced film properties to large-scale production applications. In the beginning, large banks of capacitors on the core of these HiPIMS sources made them cost-prohibitive.

Recent improvements in the HiPIMS technology made these power supplies available for research, demonstrating higher performances over DC and DCMS in various aspects. Adjusting HiPIMS process parameters like peak target current, pressure, pulse width, and magnetic field strength, the degree of ionization of the sputtered flux and the diffusional atomic processes can be controlled [2,9–14]. Most of the literature about highly ionized fluxes generated by HiPIMS reports dense and smooth films obtained with excellent control over microstructure, composition, and properties [2,12,15–26]. However, all these advantages are also accompanied by deposition rate losses, sometimes over 70% compared to DCMS and conventional magnetron sputtering operating at the same power [2,9,10,12,13,26–30]. These decreased deposition rates have shadowed the numerous advantages for HiPIMS processes delaying some industrial applications, and finding alternatives to overcome this drawback is of utmost importance. Investigations to understand the nucleation and growth on a fundamental level [8,12,15,22,31–34], applying secondary electromagnetic fields near the substrate [30,35–38], and new designs of magnetron systems [2,10,35,39] have shown possible paths to increase the deposition rate on HiPIMS processes. It is expected that additional electromagnetic fields will influence ionized species' transport from the target to the substrate; thus, the current work hypothesizes that redesigning the electromagnetic fields in HiPIMS systems can define ions' energy and trajectory to control the thin films' deposition rates. In a study, the deposition of CrB_2, Al, and Cu films by HiPIMS and using a secondary magnetic field close to the substrate and aligned to the magnetron's outer poles of the target showed enhancements up to 15% in deposition rates when comparing with DC magnetron sputtering [37]. The same authors also demonstrated another 30% rate improvement if a negative bias was applied to the substrate [37]. Other experiments have led to about 20% increases in the deposition rate of HiPIMS by using a strongly unbalanced magnetron compared to conventional unbalanced magnetrons, leading to a more confined plasma and limiting the ion losses to the walls [40].

More in-depth structural characterization analysis of the Al and Cu films obtained with secondary electromagnetic fields showed changes in crystallographic texture with preferential orientation in the direction [111] [37]. Similarly, the ceramic films CrB_2 exhibited an increase in the deposited films' hardness using the secondary coils [37]. Optimized magnetic field configurations of magnetrons assemblies aiming at low plasma impedance have shown thicker, denser, and with superior adhesion CrN and TiN coatings than coatings deposited by conventional DC magnetron sputtering or arc evaporation [41]. Nevertheless, it was also demonstrated that CrN DC magnetron coatings grew with a preferential orientation along the [111] direction while the HiPIMS along the [200] direction [41]. Therefore, adding a secondary magnetic field or optimizing the magnetron's strength systems modify the depositions rates and provide control over the structure for either DCMS or HiPIMS processes.

A higher degree of ionization of sputtered material and dissociation of gas species will lead to excellent control over the films' composition during reactive DCMS (R-DCMS) or reactive HiPIMS (R-HiPIMS). The configuration and magnetic strength modification has promoted higher ionization degrees, control of reactivity, and the magnetic fluxes will impact the trajectory and kinetic energy of the plasma species [12,29,35,41]. Several authors have investigated the topic of species distribution for DCMS and HiPIMS processes [11,33,35,42], yet the link of the resulting species distributions with the film stoichiometry, structure, and deposition rate is rarely explored. The establishment of these links will allow for coating's tunability with specific control of deposition rate, selective deposition or patterning, compositional gradients, crystal texture, or even tailoring final properties.

The present work explored the magnetic field substrate biasing correlations of Chromium-Nitrogen R-DCMS and R-HiPIMS films with the chromium ions' ionization state by *in situ* optical emission spectroscopy and their structural and morphological properties. The strong correlation of magnetic biasing with the different film aspects opens a new panorama for discovering new structures and a road to create a new advanced surface modification method for coatings-based manufacturing at nano and micro scales.

2. Materials, Methods, and Processes

2.1. Sputtering System Setup

The schematic of the magnetron sputtering system used to deposit the chromium – nitrogen (Cr-N) films onto silicon substrates is shown in Figure 1. The system is equipped with two 2-inches magnetron guns (only one is showed in Figure 1) and a sample holder stage to coat flat or powder specimens. The system can generate plasma using three options of power sources, a CESAR ® 300 W RF, an MDX ® 500 W DC, or a 2 kHz 2 kW IMPULSE ™ from Starfire Industries with the POSITIVE KICK ™ option to allow a voltage polarity inversion at the target. In addition, the RF and DC power sources can be used to electrically bias the substrate or use them as power sources to perform plasma etching at the substrate surface prior to processing. The sample holder may be continuously adjusted to change the gun to substrate vertical position and offer horizontal positions aligned to any of the guns or mid-point of both. The sample holder has also been adapted with temperature monitoring, float-ground-voltage biasing and monitoring, removable permanent magnet (magnetic biasing at the substrate), and actuators to induce vibration in powder specimens. The setup allows monitoring the plasma optical emission wavelengths at a gun-to-substrate vertical distance of 40 mm.

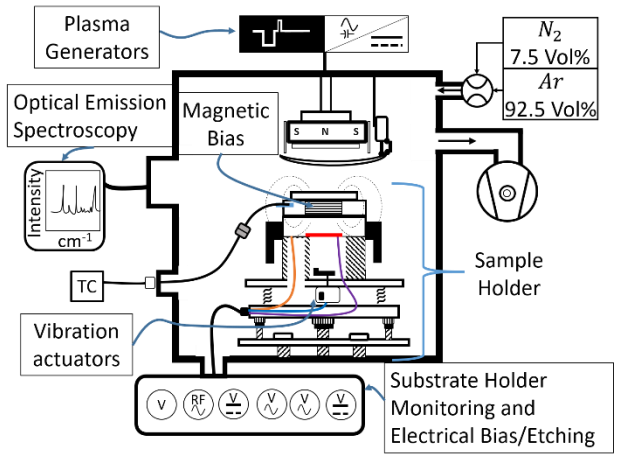

Figure 1. General sketch of the magnetron sputtering system.

2.2. Process Parameters

2.2.1. Substrate and Target Material

The films were deposited on silicon wafers substrates with nominal resistivity of 1-100 Ω cm with a crystal orientation in the direction [100]. Samples were cut to an area of about 12 cm^2, rinsed with acetone, and dried with nitrogen before located at position 1, aligned with the torus ® gun. The gun was loaded with a 2 inches chromium target of 99.95% purity. The substrate to gun distance was fixed to 80 mm. The substrate-to-ground impedance was set between 5.5 MΩ and 6 MΩ, without imposing external electrical bias allowing self-biasing.

2.2.2. Magnetic Field Details

The evolution of the structure of the films deposited by R-DCMS and R-HiPIMS subjected to a magnetic field was investigated. A permanent magnet using different orientations was placed at the substrate side to modify the magnetic field in the chamber (hereafter denoted as magnetic bias). The magnetic field of the gun and on the surface of the substrate with magnetic bias were mapped with a 475 DSP Gaussmeter from Lake Shore Cryotronics Inc. using an axial Hall probe of 4.75 mm of diameter (part number HMNA-1904-VR). Table 1 corresponds to the magnetic field measurements at the target's surface (0 mm) and a fixed gun to substrate distance of 37 mm without the substrate holder inside the system. Meanwhile, Table 2 presents the magnetic field at the substrate's surface on the holder with magnetic bias configuration before introducing it to the system. Due to geometric restrictions of the Hall probe and gun to substrate distance, the direct measurement of the magnetic field, with gun and substrate in place, could not be done. Instead, the data in Table 1 and Table 2 were used to model the magnetic field of each configuration. The calculations assumed the setup as axisymmetric around the Z-axis. The modeling was carried out using ANSYS electronics desktop 2019, and it is presented in Figure 2.

The magnetron gun consists of two permanent magnets. The shape of and orientation of the magnets corresponds to two concentric annular rings in antiparallel magnetic geometry. Only half of the magnetron magnets' cross-sections are shown at the top of Figures 2a through 2c to take advantage of the modeling's axisymmetry.

Table 1. Measurements of the magnetic field at the gun without magnetic biasing at the substrate.

Horizontal position from the center of the magnetron gun (mm)	Gun to substrate distance (mm)	Magnetic Field magnitude (mT)
-31	0	100
-31	37	6
-25	0	100
-25	37	9.04
0	0	49.2
0	37	9.77
25	0	90.9
25	37	8.85
31	0	89.5
31	37	5.38

Table 2. Magnetic field at the substrate surface with magnetic biasing.

Horizontal position from the center of the magnet (mm)	Magnetic field (mT)
-12	235
0	98
12	228

The modeling and experiments were carried out using three different magnetic configurations in the system. The first configuration shown in Figure 2a does not use any permanent magnet at the substrate, and it is denoted as NM, which is the conventional configuration used in magnetron sputtering. In the NM configuration, the field lines generated in the inner ring closes in the outer one, but not all the lines generated on the outer annular ring pass through the central magnet. The other two configurations

presented in Figure 2b and Figure 2c use a permanent N52 neodymium magnet with a cylindrical shape of 14.75 mm of radius and 5.66 mm thickness behind the substrate surface. In the configuration described in Figure 2b, the substrate magnet poles are aligned with the gun's central magnet, and it is denoted as MT. Then, the field lines generated on the substrate's magnet close on it without pairing with those from the magnetron gun. The configuration in Figure 2c is denoted as MII since the magnet poles are flipped from the MT setting and are now aligned with the gun's outer poles. The field lines of the MII configuration pair with some of the ones from the gun's outer magnet. The estimated field lines at the surface of the substrate in each magnetic setup (assuming the whole setup of gun and magnetic bias) are shown in Figure 2d. It is observed from the plot that distribution of field lines across the substrate surface is constant for the NM configuration and almost antisymmetric for MT and MII configurations.

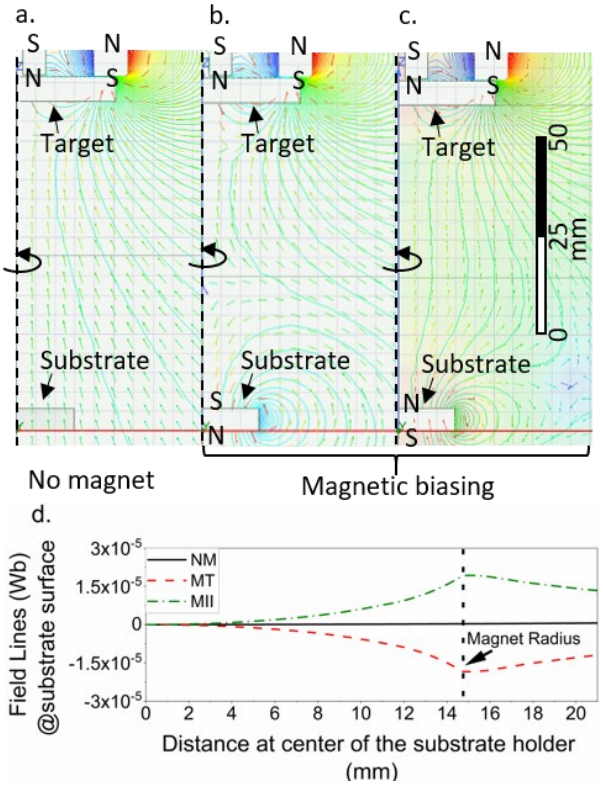

Figure 2. The magnetic field for each set of experiments. a. No magnet in the substrate holder, NM configuration. b. magnetic biasing MT configuration. c. magnetic biasing MII configuration. d. Magnetic field lines at the surface of the substrate.

2.2.3. Plasma Generation and Deposition Monitoring

The effect of magnetic biasing on the deposition rate, morphology, structure, and composition of Cr-N films on Si substrates prepared by reactive DC and high power impulse magnetron sputtering deposition techniques was studied. The samples prepared by R-DCMS will be identified with the prefix DC while the ones prepared by R-HiPIMS with the prefix HP. A total of six combinations of plasma generator and magnetic configurations were deposited with an average power of 100 W for 20 minutes at room temperature. For the deposition processes, the chamber was evacuated to a base pressure of 1E-6 Torr or below. Then, a gas mixture of 7.5 volume % of nitrogen in argon was used to set the pressure to 15 mTorr. The concentration of nitrogen in the gas mixture was selected to minimize the target-poisoning effect.

The operation voltages for the R-DCMS processes were set in the range of 335 V to 348 V in the power control function. The voltage, current, and power data were obtained from the MDX-500 internal measurement. While the delivered power is treated as time-independent for the R-DCMS processes and set to a continuous voltage, four time-dependent steps were configured in the R-HiPIMS processes. Sputtering pulse (SP) set to 850 V by 65 µs with low output impedance, delay to positive pulse (DP) set to 4 µs at high output impedance, positive pulse (PP) set to 150 V by 20 us with low impedance and after-pulse (AP) at high output impedance. The HiPIMS power was controlled by varying the after-pulse width ranging it from 98.9% to 99.3% of the whole cycle's period. During the monitoring of the HiPIMS processes, a TA-271 Pico passive probe in a digital differential oscilloscope Pico 4444 was used to measure the voltage and current waveforms on the monitoring ports of the IMPULSE™. Similarly, for R-DCMS and R-HiPIMS

setups, the substrate-to-ground voltage was registered using a 442 Pico passive probe with an attenuation of 25:1.

The plasma species were monitored through a quartz viewport using a 600 µm fiber optic attached to a collimator located approximately in the middle point between the target and the substrate. The distance from the viewport to the center of the axis between the target and the substrate is ~ 165 mm. The optical emission spectra (OES) were registered using an Ocean Optics FLAME spectrometer in a wavelength range of 270 nm to 550 nm and an optical resolution of 1.69 nm. The estimated attenuation for the optical setup can be observed in the supplementary data Figure A.1.

2.3. Films Characterization

The chemical analysis was carried out by X-ray photoelectron spectroscopy and X-Ray Diffraction. The XPS spectra were collected in a PHI VersaProbe III with a monochromated Al k-Alpha X-ray source set it up to 200 µm spot and 50 Watts. The survey scans were gathered with a pass-energy of 280 eV with 1 eV step, while the high-resolution spectra used a pass-energy of 26 eV and 0.05 eV step. The XPS step time was held to 20 ms in all measurements. All analysis positions were pre-sputtered by 3 minutes with Ar before collecting the XPS spectra. The spectra were corrected using the carbon adventitious signal at 284.8 eV. The data was analyzed using CasaXPS software version 2.3.22PR1.0. The grazing incidence X-Ray Diffractograms (GIXRD) were obtained in an EMPYREAN MULTIPURPOSE X-RAY Malvern Panalytical diffractometer with a Cu X-Ray tube. All GIXRD were collected with an ω incidence angle of 7.5° and 0.05° 2θ step size.

Cross-sectional images at various substrate locations were used to measure coating thicknesses and to evaluate the structure. The cross-sections and lamellas across the surface of the films of each configuration were prepared using a dual focus ion beam and scanning electron microscope FIB-SEM AURIGA from ZEISS. A platinum coating protected the surfaces during milling a groove of 10 µm width and

5 µm depth. The cross-sectional FIB-SEM images were done at an angle of 54°, leading to an x:y pixel aspect ratio of 1:1.236. Each thickness evaluation included at least six measurements using ImageJ V1.52a.

The Cr-N films' surface was evaluated using a SU-70 field-emission scanning electron microscope (FE-SEM) from Hitachi. The transmission electron microscopy (TEM) and selective area electron diffraction (SAED) used in the DCMII were done in a JEOL JEM-F200 at 200kV and with a camera length of 500 mm. All electron microscopy images were processed with ImageJ V1.52a.

Additional texture measurements were done by X-ray diffraction in the EMPYREAN MULTIPURPOSE X-ray Malvern Panalytical diffractometer. The chosen crystallographic Bragg reflections for the pole figures were (200), (110) for Cr (ICDD 00-001-1250), and (111), (200), (220) for CrN (ICDD 00-011-0065). The intensity of the Bragg reflection was measured by sweeping φ azimuth angle from 0 to 360, and χ polar tilting angle from 0° to 75°, both with a step size of 3°. The pole figures were processed and plotted using a python algorithm and OriginPro 2021.

3. Results and Discussion

The fixed deposition time of 20 min and power of 100 W for both DCMS and HiPIMS with the three magnetic configurations allows for a straight comparison of samples. The process monitoring section provides information about the plasma species and the impact of magnetic biasing on the deposition dynamics. Then, a comprehensive coatings characterization is presented and evaluates multiples aspects of the chemistry, deposition rate, morphology, and structure associated with the combination of plasma generator and magnetic configuration.

3.1. Process Monitoring

The waveforms showed in Figure 3a, Figure 3b, and Figure 3d account for the delivered voltage (V_D), current (I_D), and power through the target (P_D), respectively. Figure 3c corresponds to the self-bias voltage

at the substrate (V_S) due to the interaction of its surface and the plasma. An alternative representation of Figure 3 is available in supplementary data Figure D1. During the R-HiPIMS processes, the oscilloscope's trigger has been set to register the SP, DP, PP steps, and partially the AP step until the voltage and current returned to zero. For the R-DCMS processes, the voltage and current in Figure 3 have been chosen arbitrarily with the same 250 μs span of the R-HiPIMS waveforms.

The voltage shape in Figure 3a states that the power control in the R-DCMS processes held the voltage at the target at less than half of the SP voltage set in the R-HiPIMS processes. The target voltage waveform for the three HiPIMS processes follow the same shape during the SP,DP and PP, but decays differently to zero during the AP step, having HP NM the longest decay time and HP MII the shortest one. From the current at the target in Figure 3b, it was observed that the R-HiPIMS processes during the SP step were three orders of magnitude higher than in the R-DCMSs. Among the R-HiPIMS processes, HP NM held the lowest peak current and power. All processes hold the same average power of 100 W; however, the peak power for the R-HiPIMS processes in Figure 3d is three orders of magnitude larger than the R-DCMS ones with the same conditions. In Figure 3c, the self-bias effect in the DC samples is a continuous negative voltage at about -7 V, but the HP samples evolved in five stages. In the first microseconds of the SP step, the HP samples charge negatively. The inset in the top right of Figure 3c shows that HP NM reached the highest negative biasing among the three in this first charging stage. Above 30 μs, the voltage at the substrate trended to stabilize at the same voltage of the DC samples. During the positive pulse at 150 V in the target, the self-bias voltage at the HP substrates flipped polarity too and trended to stabilize at 140 V. However, the voltage at HP NM sample was faster flipping polarity in the first microseconds of the PP step, or decaying to zero during the AP step.

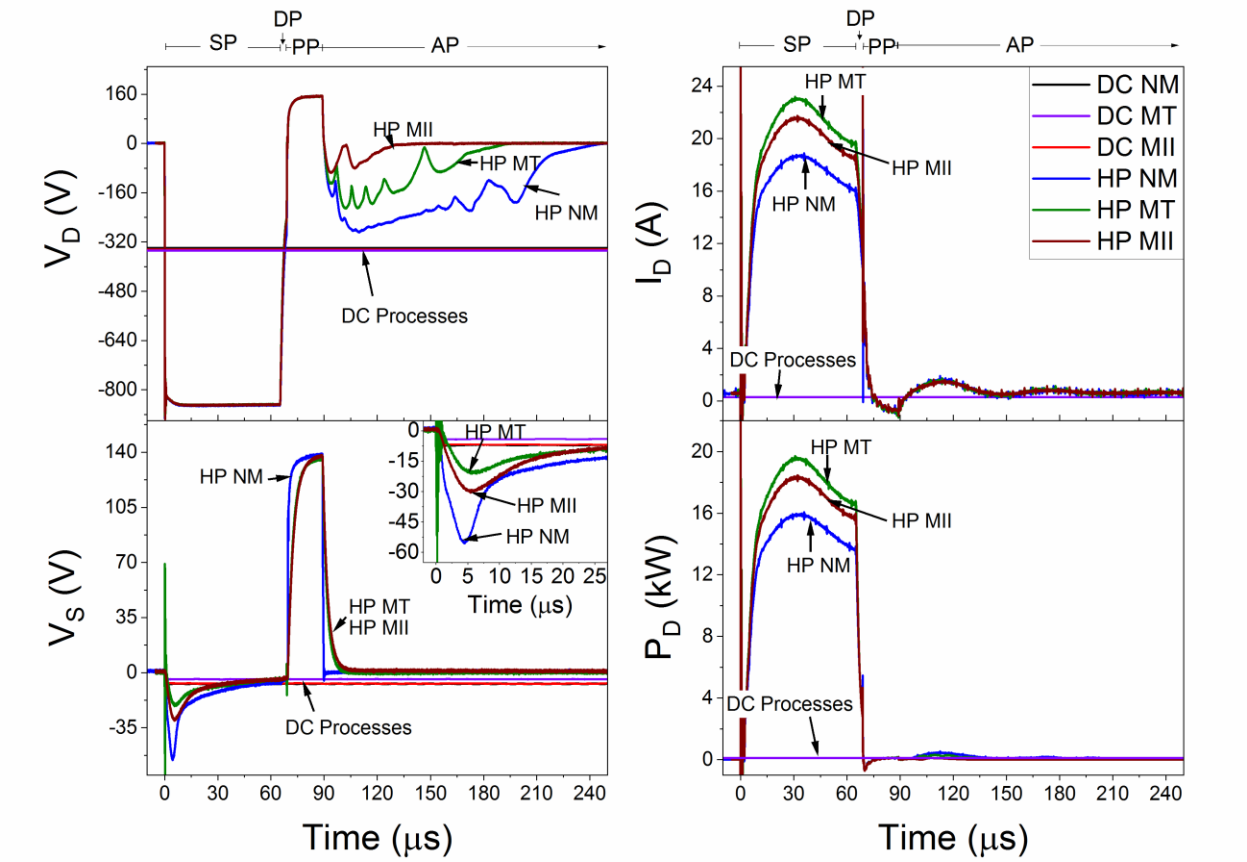

Figure 3. a. Discharge Voltage (V_D). b. Discharge Current (I_D). c. Voltage at the substrate (V_S). d. Power at the target (P_D). During sputtering pulse (SP), delay to positive pulse (DP), positive pulse (PP), and after-pulse (AP).

Table 3 summarizes the peak power and average energy released through the plasma generator in each pulse step (calculated as the area under the curve of the power waveform in Figure 3d). At the SP step, the released energy was almost three orders of magnitude lower for the R-DCMS processes than for any of the R-HiPIMS processes. On the other hand, during the first 400 μs of the AP, the highest released energy was for HP NM and the lowest for HP MII among the HP processes. This latter result is coincident with the voltage decay length observed in Figure 3a. However, it is essential to notice that these waveforms depend on the combinations of the species excitation and decay, and the different output states and impedance of the plasma generator. Therefore, the analysis of these curves can only give

qualitative information about the plasma dynamics due to the involvement of the output stage of the plasma generator.

Table 3. Peak power and average released energy in each pulse step.

Sputtering Pulse (0 µs to 65 µs)				
Process	DC NM, DCMT & DC MII	HPNM	HPMT	HPII
Peak Power (kW)	0.10	16.08	19.71	18.47
Released energy pulse (J)	6.44E-03	8.83E-01	1.07E+00	1.01E+00
Delay and Positive Pulse (65 µs to 89 µs)				
Process	DC NM, DCMT & DC MII	HPNM	HPMT	HPII
Released energy pulse (J)	2.40E-03	2.75E-02	3.02E-02	2.89E-02
After-Pulse (89 µs to 500 µs)				
Process	DC NM, DCMT & DC MII	HPNM	HPMT	HPII
Released energy pulse (J)	4.11E-02	2.14E-02	9.51E-03	1.68E-03

Figure 4 presents the optical emission spectra for the processes under analysis. However, before jumping into the scrutiny of relative intensities, it is crucial to consider the optical attenuation shown in the supplementary data Figure A1, particularly in the range of 270 nm to 360 nm. All spectra in Figure 4 have been normalized to the peak at 520.7 nm. The emission intensity peaks at 284.32 nm and 313.20 nm are related to Cr(+) species. The emission peaks at 302.19 nm, 426.20 nm, 435.03, and 520.70 nm were identified as Cr(0) species. While the N_2 species were identified by the headbands of the second positive system N_2(0)at 315.93 nm and 337.13 nm, and N_2(+) charge species by the first negative system at 391.44 nm [43,44].

Overall, all the R-DCMS processes showed Cr(0) as the predominantly existing target species in the plasma except for the presence of small Cr(+) peaks at 284.32 nm and 313.20 nm in DC MII (inset for DC MII in Figure 4). As expected, all the R-HiPIMS processes showed a combination of both Cr(0) and Cr(+) species.

Even more, the intensity of the Cr(+) emission peak at 313.2 nm for HP MII was stronger than the Cr(0) emission peak at 520.7 nm. Another critical observation for R-HiPIMS processes, in general, is the appearance of relatively high-intensity $N_2(0)$ peaks at 315.93 nm and 337.13 nm.

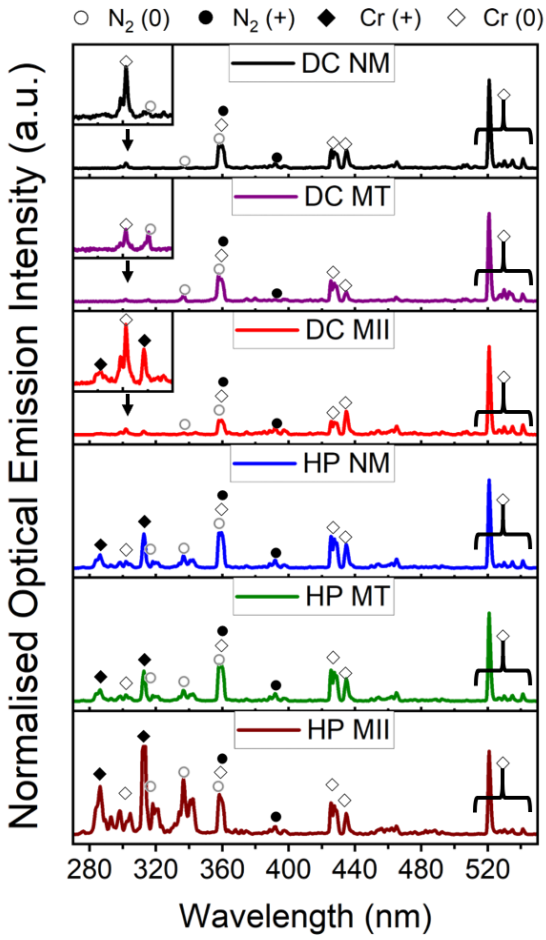

Figure 4. OES plasma spectra for all sputtering processes with identification of nitrogen and chromium species. The insets at DC spectra correspond to a zoom in in the range of 270 nm to 330 nm.

The results in Figure 3, Table 3, and Figure 4 evidence the affectation of the plasma species and ionization of sputtered material due to magnetic biasing for both R-DCMS and R-HiPIMS processes. The voltage decay at the target in Figure 3a during the AP step for the R-HiPIMS processes with magnetic biasing is faster than without it. This decay may be due to a shorter lifetime of the species once the generator

switches to high impedance. The field shape in Figure 2c may configure a magnetic confinement bottle for the MII configuration that increases the collision among the species in the bulk of the plasma, leading to a higher ionization during the SP step and a faster decay during the AP step. This ionization route may explain the enhanced intensity of the Cr(+) peaks in the HP MII process and their detection in the DC MII in Figure 4. On the contrary, the field in Figure 2b for the MT configuration shows that the magnetic shape may leak charged species from the bulk of the plasma towards the vessel walls, ruling out a higher ionization. A second feature is the observed self-biasing effect at the substrate in Figure 3c. The substrate surface charges electrically due to the arrival of ions and electrons during sputtering deposition [3,5,28,45–48]. However, the substrates in HP NM were more negatively biased during the SP step, and they were the first to flip polarity during the PP step. During the SP step, the negative voltage at the target pulls all cations, and mostly electrons reach the substrate, but during PP step the positive charge species are kicked out from the target and reach the substrate inverting its polarity [11,35,42,48,49]. Therefore, the lower electrical charge for the magnetically biased samples can be related to a lower charge particle flux at the substrate.

The magnetic flux in Figure 2d predicts a distribution of magnetic field lines at the substrate surface for HP MII and HP MT configurations that may reflect a fraction of the charged particles from the substrate to the bulk of the plasma [50,51]. This assumption is consistent with the self-biasing curves for the R-HiPIMS processes seen in Figure 3c. This reflected species may thermalize the species in the plasma bulk and boost the ionization of sputtered material observed in HP MII spectrum and DC MII inset in Figure 4. However, the increased ionization of sputtered material for sample DC MII is still negligible because of the low electron density in R-DCMS processes compared to R-HiPIMS processes.

The effect of magnetic biasing may be explained using the schematic representation given in Figure 5. Relevant mechanistic events are highlighted with roman numbers. Particularly the events (I) through (VI) have been described by other authors in the context of DCMS and HiPIMS processes [27,40,52,53], while

the events (IV), (VI), (VII), and (VIII) should be adapted to the magnetic biasing case. As stated before, the clever design of a magnetron sputtering gun increase the path length of electrons during the plasma discharge, enhancing the probability of collisions with gas molecules [5,8]. These collisions lead to gas ionization (I). The newly gas ionized species can be accelerated to the target surface. The impact of the ions on the target surface may produce secondary electrons that feed the electric discharge, may sputter surface atoms (II), may lead to species implantation and target poisoning, or may recombine and bounce, returning to the bulk of the plasma (III) [4,54,55]. The sputtered target species travel through the plasma bulk and may reach the substrate surface (IV). The sputtered material may be ionized while crossing the plasma if the electron density is high enough, typical conditions in HiPIMS discharges. Depending on the kinetic energy of this ionized material, these ionic species may runaway and become part of the film deposition on the substrate (IV), be lost sideways at the reactor's walls [40,52,53], or be accelerated towards the substrate leading to self-sputtering (V) [27,56] or target poisoning [8,17,52,55]. The collision of gas and sputtered species, neutral and ionic, thermalize the plasma bulk and may lead to gas rarefaction (VI) [4,8,52,55,57]. The magnetic biasing adds mirroring and confinement effects. In both MT and MII configuration (refer to Figure 2b and Figure 2c), the magnetic field configuration reflects the electrons and ion species from the substrate towards the plasma bulk (VII). This reflection effect can enhance the collisions between species with further thermalization of the plasma (VIII) or enhancement of the ionization rate.

In the MII configuration, the field lines indicate a magnetic confinement bottle that explains the enhanced ionization. In the case of MT, the divergent shape of the magnetic field configuration allows species to leak towards the reactor walls, and the electron density may not be high enough to affect the ionization process of sputtered material. In fact, the OES spectra in Figure 4 reveal ionization enhancement for DC MII or HP MII but no for DC MT or HP MT. Similarly, magnetic biasing may affect the neutral species excitation process due to an increased collision rate suggested by the waveforms in Figure 3, but it was

not corroborated in this work by any method. Finally, these phenomena are expected to affect the deposition flux (IV). The altered magnetic field of the magnetic biasing will influence the ionic or excited sputtered species differently. Since magnetic biasing has a mirroring effect in the ionic species, the deposition rate of these species will drop in the two options discussed in this paper. On the other hand, the magnetic field will interact with the magnetic moments of the neutral metal species (Me) [58], and if this interaction is strong, the deposition flux will be affected. The magnetic confinement bottle in the close option MII may guide the metal species with high magnetic moments towards the substrate [58–61].

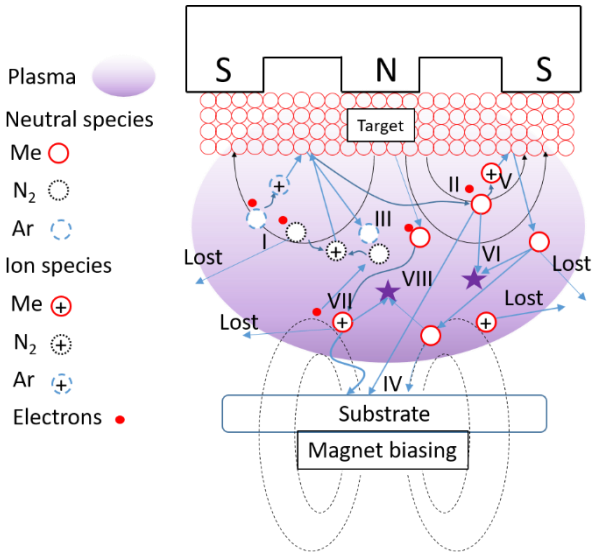

Figure 5. Schematic representation of the sputtering processes with magnetic biasing.

3.2. Chromium-Nitrogen Bond

The XPS analyses of DC NM, DC MT, HP NM, HP MT, and HP MII samples were performed at three random locations and uncertainty is given by the standard deviation of the three measurements with one decimal place. In addition, a more detailed analysis was performed for the DC MII sample since it evidenced two concentric circles with a radius of about 4.9 mm and 15 mm (supplementary data Figure B1 and B2g). Thus, two measurements were taken at the center of the sample (~0 mm), two right after the first circle

(~6 mm from center), and two beyond the magnet´s radius (~17 mm from center). The survey scans revealed that all samples principally contained Cr, N, and O, and their composition in atomic percentage is summarized in Table 4. The HP samples contained more nitrogen and less oxygen than the DC samples. Among the DC samples, DCMT sample led to the highest atomic percentage of nitrogen, while in HP samples were similar with slightly higher N content for the magnetic-biased samples.

Table 4. Films composition measured by XPS survey scans.

SAMPLE		Atomic Percentage %						Cr/N ratio
ID	Position	Cr		N		O		
DCNM	N/A	56.7 ±	0.7	16.9 ±	0.2	26.5 ±	0.5	3.36
DCMT	N/A	47.4 ±	2.5	26.5 ±	1.9	26.1 ±	4.2	1.79
DCMII	CENTER	56.9 ±	1.0	21.2 ±	1.3	21.9 ±	0.2	2.68
	MIDDLE	63.4 ±	1.2	21.1 ±	0.1	15.5 ±	1.2	3.00
	OUTER	73.4 ±	0.6	18.8 ±	1.1	7.9 ±	0.5	3.90
HPNM	N/A	54.0 ±	1.2	37.1 ±	0.9	8.9 ±	0.6	1.45
HPMT	N/A	53.0 ±	0.9	39.3 ±	0.6	8.5 ±	1.1	1.35
HPMII	N/A	53.5 ±	0.5	38.5 ±	0.2	8.4 ±	0.5	1.39

Figure 6 presents the high-resolution XPS spectra for chromium and nitrogen. For the DCMS samples, the $Cr2p_{3/2}\ to\ Cr2p_{1/2}$ doublet separation was 9.33 eV ± 0.02 eV, and the high-resolution N1s peak was centered at 397.27 eV ± 0.23 eV. In the HiPIMS samples, the chromium doublet separation expanded to 9.45 eV ± 0.01eV, and the N1s peak shifted to 396.70 eV ± 0.10 eV.

The doublet separation for $Cr2p$ of 9.30 eV and 9.45 eV are related to metallic chromium and chromium nitride (CrN), respectively [62,63]. Similarly, the XPS high-resolution nitrogen peaks for the DC samples suggest that the nitrogen is in solid solution with the chromium [64–67]. However, nitrogen peak shifting in the HP samples is often assigned to nitrides in the form of CrN [64–67]. Additionally, other small peaks further demonstrated that DC samples may have some N-H bonds or C-N bonds and N-H bonds or N and Cr in solid solution for the HP samples [68,69].

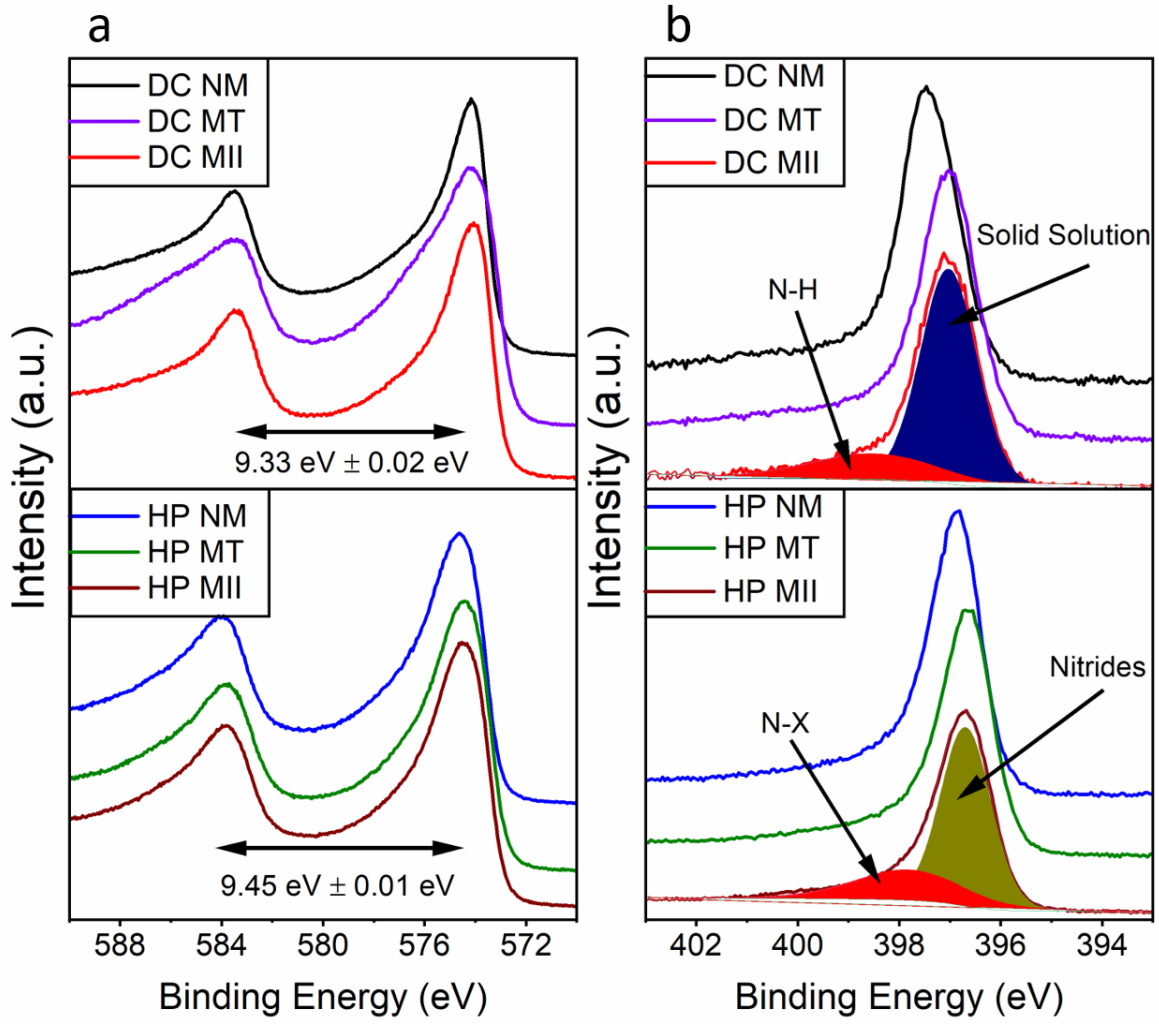

Figure 6. The high-resolution XPS spectra for a. Chromium and b. Nitrogen.

Figure 7 presents the GIXRDs for all the prepared samples. The DC samples exhibited broad peaks primarily identified as chromium (200), and the HP samples revealed peaks associated with CrN, validating the chemical analysis provided by XPS. The diffractograms were shifted with respect to the ICDD standard patterns for body-centered cubic (BCC) chromium (00-001-1250) and face-centered cubic (FCC) chromium nitride (00-011-0065). The DC samples mainly shifted to lower 2θ angles while the HP samples shifted to higher angles.

The GIXRD peak analyses are presented in Table 5. The lattice parameter (a') has been calculated for each XRD reflection. The HPs' corrected lattice parameters (a N-R) were obtained using Nelson-Riley method [70,71], but dismissing the chromium nitride (200) peak due to the possibility of convolution with the chromium (110) reflection. The data in Table 5 shows expansion in chromium body-centered cubic cell for the DC samples, and a contraction in the chromium nitride face-centered cubic cell for the HP samples.

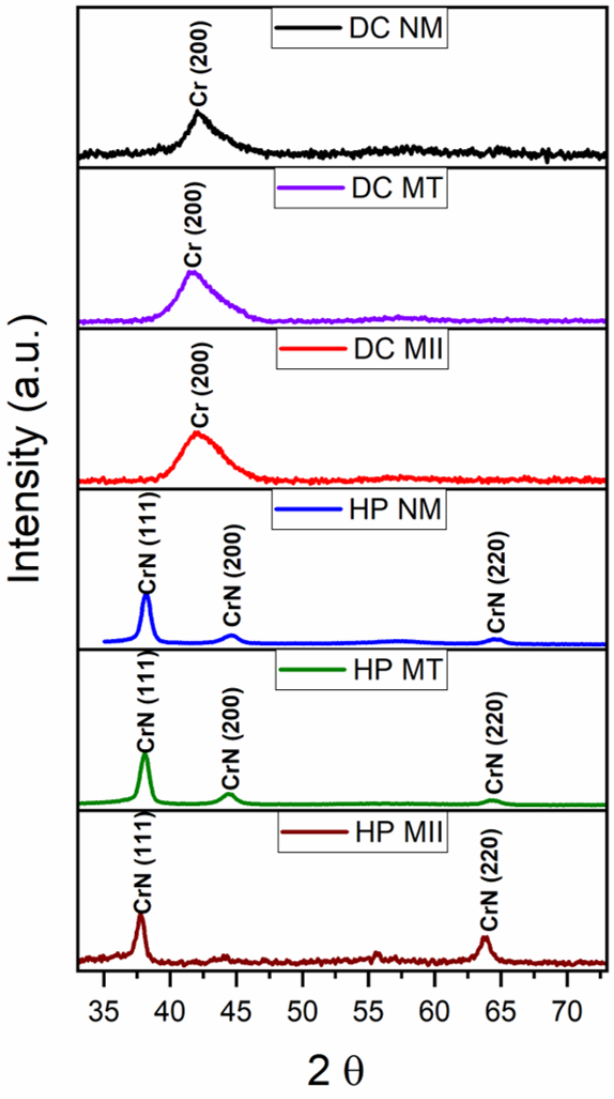

Figure 7. Chromium and chromium nitride grazing incident x-ray diffraction for R-MSDC and R-HiPIMS processes.

Table 5. XRD peak identification and calculated lattice parameter

SAMPLE						ICDD Standard			
ID	**2 ɵ**	**FWHM**	**d (Å)**	**a' (Å)**	**a N-R (Å)**	**Compound**	**hkl**	**d (Å)**	**a**
DCNM	42.5	3.09	2.13	3.01	N/A	Cr	110	2.05	2.90
DCMT	42.1	3.56	2.15	3.03	N/A	Cr	110	2.05	2.90
DCMII	42.4	3.52	2.13	3.01	N/A	Cr	110	2.05	2.90
HPNM	38.2	0.891	2.36	4.08	4.07	CrN	111	2.39	4.14
	44.6	1.39	2.03	4.06			200	2.07	
	64.6	1.07	1.44	4.08			220	1.46	
HPMT	38.1	0.789	2.36	4.09	4.08	CrN	111	2.39	4.14
	44.4	1.27	2.04	4.08			200	2.07	
	64.4	1.11	1.45	4.09			220	1.46	
	77.5	1.472	1.23	4.08			311	1.25	
HPMII	37.7	0.805	2.38	4.13	4.12	CrN	111	2.39	4.14
	63.8	0.993	1.46	4.12			220	1.46	

The 2θ peak shifting and the wide FWHM observed for DC samples can be related to the induced disorder and strain due to nitrogen diffusion in the Cr BCC structure. In the case of the HP samples, the shift to higher 2θ angles can be due to the nitrogen vacancies in the CrN FCC structure. Nonetheless, the broad peak found around 44.5-2θ for HP samples may also indicate the partial presence of Cr BCC phases.

Table 6 presents the estimated calculation of nitrogen saturation in both Cr and CrN structures to understand the effect of nitrogen content in the lattice. The calculations were carried out based on Vegard's law mathematically expressed in equation (1).

$$a_{A_{1-x}B_x} = (1-x)a_A + xa_B \qquad (1)$$

The Cr BCC lattice can hold up to ~33 at.% of nitrogen before transforming into hexagonal Cr_2N. Assuming this saturation limit and occupancy of the tetrahedral interstitial sites of the BCC structure, the fully saturated lattice parameter would be 3.04 (Å), and 2.90 (Å) for no nitrogen. Similarly, for the CrN FCC

structure, the fully saturated lattice parameter is 4.14 (Å), but it would be 3.62 (Å) with no nitrogen in the structure. The nitrogen saturation column presented in Table 6 is consistent with the higher incorporation of nitrogen in the magnetically biased samples, complementing the XPS results given in Table 4. These data confirm the different outcomes already mentioned about R-DCMS and R-HiPIMS processes; mainly, the increased nitrogen reactivity in HiPIMS that promotes the formation CrN phase [8,72–76].

Table 6. Chromium to Nitrogen presence in the films calculate by Vegard's law.

SAMPLE			Nitrogen
ID	**Phase**	**Lattice parameter (Å)**	**saturation%**
DCNM	Cr BCC	3.01	75%
DCMT	Cr BCC	3.03	93%
DCMII	Cr BCC	3.01	79%
HPNM	CrN FCC	4.07	87%
HPMT	CrN FCC	4.08	89%
HPMII	CrN FCC	4.12	96%

3.3. Thickness and deposition rates

Samples were cross-sectioned at different radial locations from the center point, coincident with the center axis of the target and the center of the biasing magnet when present. Figure 8 contains the thickness measurements across the surface for the whole set of experiments. Based on the visual appearance of the DC MII sample, three locations have been highlighted in Figure 8, center/C (at ~0 mm of the center), inner ring/IR (at ~4.9 mm of the center), and outer ring/OR (at ~14 mm of the center). In general, the DC samples were at least two times thicker than the HP samples under the same conditions. As a reference, the measured thickness for samples deposited with no magnetic bias was 804 nm for the DC NM samples and 332 nm for the HP NM samples, with a variation of thickness across the surface of ~4% and ~3%, respectively. The DC MT thickness was close to the reference DC NM, while the HP MT thickness was about 360 nm with variations across the surface of ~7% and ~5%, respectively. Meanwhile, the thickness of the DC MII sample was 2790 nm at the center of the sample holder, 272% thicker than at

22 mm of the center. On the contrary, the HP MII sample showed a thickness of around 246 nm at the center and 273 nm at 20 mm, giving a total variation across the surface of ~ %14.

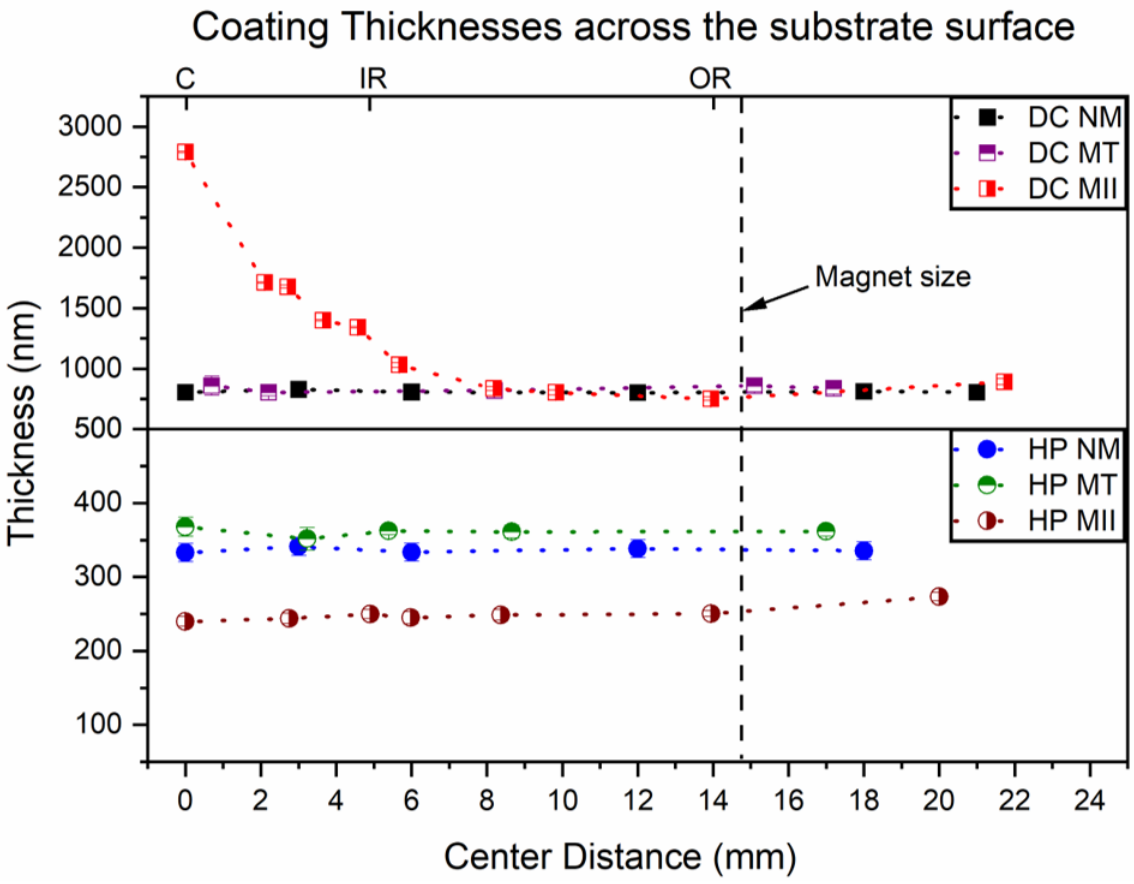

Figure 8. Thickness of the films across the substrate surface from the magnet center towards the outer radius.

The deposition rates were calculated by dividing the thickness over deposition time, although this calculation must be carefully considered for DC MII due to the induced inhomogeneity. DC NM demonstrated a deposition rate of 0.76 nm s^{-1} and HP NM of 0.27 nm s^{-1}.

The deposition rate of the magnetic configuration DC MT did not show variation in the deposition rate with respect to DC NM, but the DC MII samples with magnetic biasing were highly impacted. The DC MII sample showed no increase in the deposition rate with respect to the DC NM sample at the outer region,

> 10 mm from the center. However, the inner region shows a steep increase in the deposition rate, peaking at the center with about 2.41 nm s^{-1}. This represents more than a three-fold increase from the outer to the inner region. Indeed, these changes in sputtered material flow can lead to different structures. However, a counter phenomenon was observed in the HiPIMS samples with magnetic biasing. The deposition rates with magnetic biasing showed an increase of about 11% for the HP MT configuration and a decrease of about 34% with the HP MII configuration.

As discussed in section 3.1, the magnetic field may impact the ionization process, the flow, and the energy of the incoming plasma species [4,10,35,38]. The thickness homogeneity of the samples may be explained using the excitation mechanism proposed in Figure 5. The electron configuration of the ground state of Cr ([Ar] $3d^5 4s^1$) offers six unpaired electrons leading to a strong magnetic moment [77]. Similarly, the several excited Cr species that may appear due to plasma species collision and excitation decay will have strong magnetic moments that interact with the magnetic field in the biasing configurations, and the transport of Cr ions species will be affected by resulting Lorentz forces [77–79]. The magnetic flux distribution in Figure 2 suggests that the magnetic field may guide the Cr species towards the center of the substrate holder, increasing their deposition rate, but the mirroring effect on the ionic species may decrease it. Since the ionization ratio of the sputtered material in the DC MII process is still low in comparison with the HiPIMS processes, but it was enhanced regarded to the DC NM process, the deposition flux of neutral excited species may be boosted at the center of the holder as shown in Figure 8. In the case of the MT configurations, there was insufficient evidence of significant change in the ionization or excitation of the Cr species. These may be the reason for the negligible effect in the deposition flux in the DC MT configuration. However, this research did not perform a detailed study about the plasma speciation and pairing the information with their magnetic moments and their effect on deposition flux. Finally, the ionization process of sputtered Cr in the HP MII process impaired the deposition rate at the center of the sample due to the reflection of the charged species, while it may have a slight increment outwards the

magnet radius where the mirroring effect is lower than in the center. It is still intriguing how the different configurations affected the total deposition rate, particularly the HiPIMS processes.

3.4 Structural Morphology of R-DCMS Samples

The top-view and cross-sectional images of the DC NM and DC MT are presented in Figure 9, and the DC MII sample is separately shown in Figure 10. All three samples evidenced columnar growth. However, the DC NM and DC MT samples featured nodular tops with an average size of about 35 nm and 39 nm, while the DC MII exhibits several morphologies.

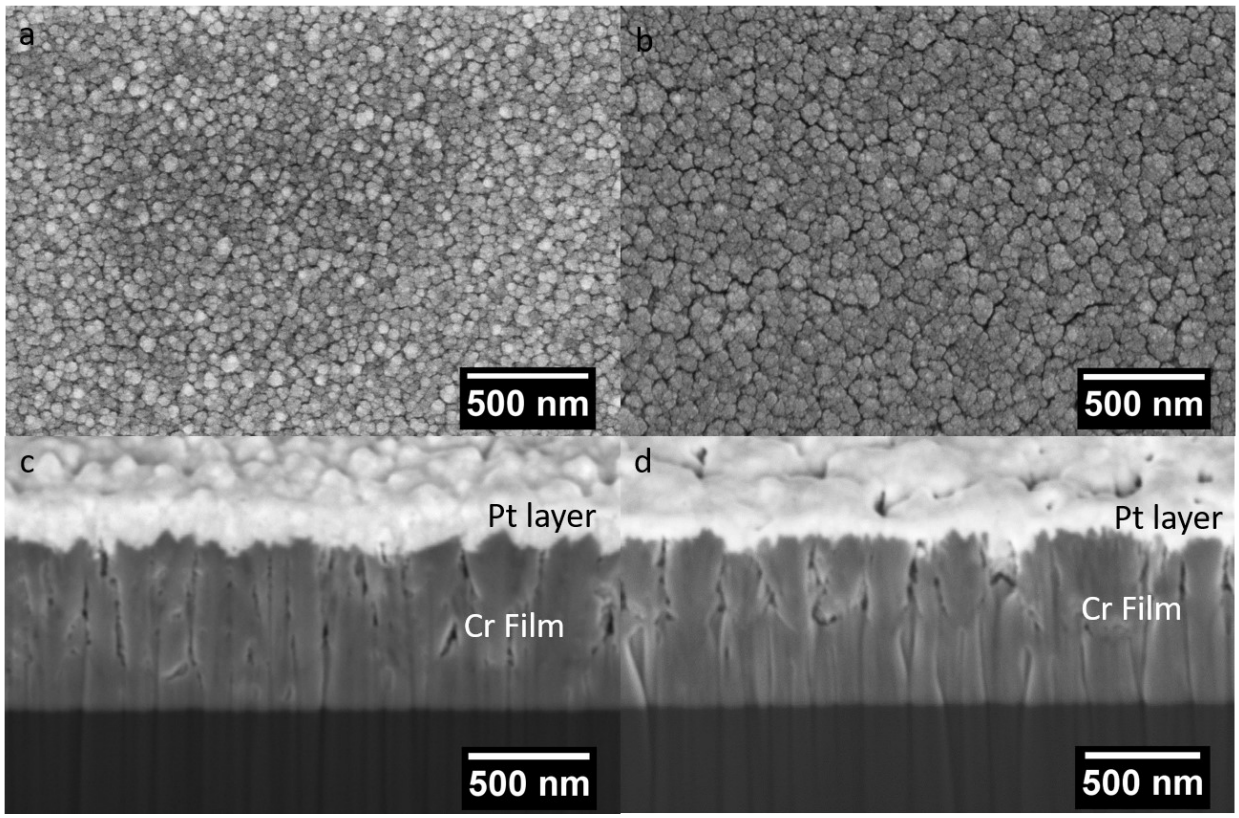

Figure 9. Surface and cross-section of the DC NM and DC MT samples. a. surface of DC NM. b. surface of DC MT. c. cross-section of DC NM. d. cross-section of DC-MT.

The DC MII sample characteristics varied across the surface; the thickness, morphology, and structure of the films differed depending on the location measure from the center radially. The SEM images of the

surface at eight radial locations can be observed in supplementary data B2. Figure 10 compares the surface SEM images, the TEM cross-section images, and the SAED patterns of three locations across the surface of the DC MII sample. The three cross-sectional locations correspond to C, IR, and OR positions marked in Figure 8.

The structure at the center of DCMII corresponded to a highly packed columnar growth with a strong out-of-plane crystal texture in the [002] direction of the Cr BCC. The structure at ~4.9 mm of the center is also columnar and highly packed, but the texture of the grains has some precession around the out-of-plane direction. At the outer location at ~14.0 mm of the center, the SEM image identifies voids among the columns visible in the TEM cross-section image. On the other hand, the SAED pattern in Figure 10 for the outer location does not present a crystal texture. Instead, it has shown continuous rings typical of randomly oriented polycrystals.

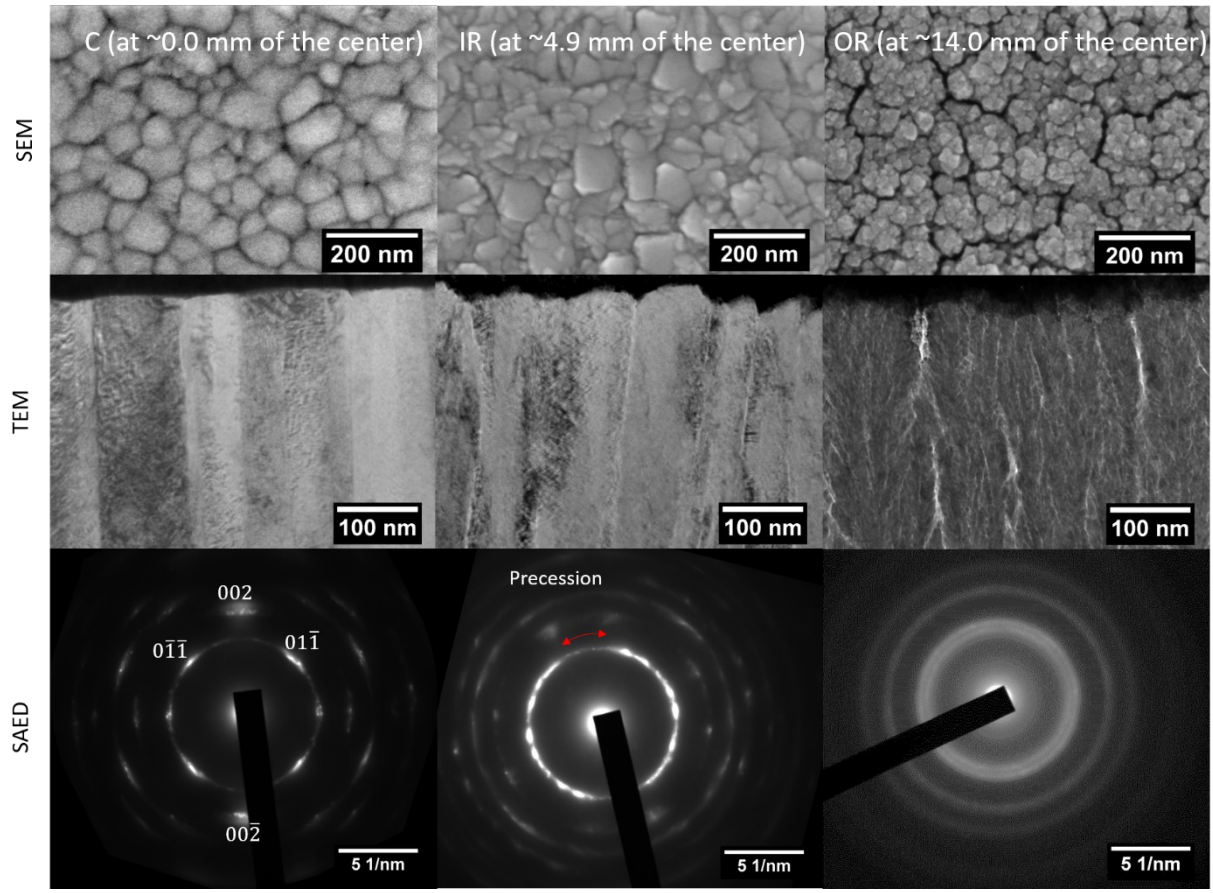

Figure 10. Structure of the DC MII film at the center (C), at 4.9 mm of the center (IR) and 14.0 mm of the center (OR).

The SAED patterns in Figure 10 were carried out on an illuminated circle about 540 nm in diameter. These SAED may correspond to a low sampling of grains for the texture analysis. However, XRD texture measurements and the multiple columns that will fit in the irradiated area rule out the issues with the sampling.

DC NM and DC MT samples did not exhibit a detectable preferential orientation by the XRD setup; therefore, the poles figures were not included in the core data of the present work, but they can be found in the supplementary data Figure C1 and Figure C2. Figure 11 shows the XRD pole figures and crystal texture analysis performed for the DC MII in two positions.

In both cases, the setup swept for the X-Ray intensity for the chromium (ICDD 00-001-1250) reflections (002) and {011} in the χ and $\emptyset$ angles. The DC MII/C (002) and {011} pole figures in Figure 11 correspond to the alignment of the irradiation with the C position. The $\chi = 0$ tilting position marks the diffraction vector coincident with the normal to the surface or out-of-the plane direction. The strong X-ray reflection peak intensity in the DC MII/C (002) pole figure confirms the out-of-the-plane texture of the Cr BCC crystals. Similarly, the ring shape of the DC MII/C {011} pole figure suggests the rotation of the BCC crystals around the axis in the direction [002].

The second irradiation position corresponds to alignment with the IR position. The (002) reflection was unclear in the pole figure and was excluded from this work. The crystal factor for the (002) reflection induces a low intensity on the XRD patterns unless it is highly texturized. However, the DC MII/IR {011} pole figure is still appreciable. The ring shape of the C counterpart is now deformed. The loss of the ring shape may be due to the precession of the BCC crystals. The cubic structure of Cr will lead to {011} diffraction peaks at tilted angles of the reflection (002) of 45^{o} and 90^{o} angles. The XRD reflection profile

in the tilting χ direction for Cr {011} in Figure 11, shows symmetric peak intensity reflections at 45° tilts for the irradiation at C, but the peak reflections shifted to 21° and 33° in the IR position.

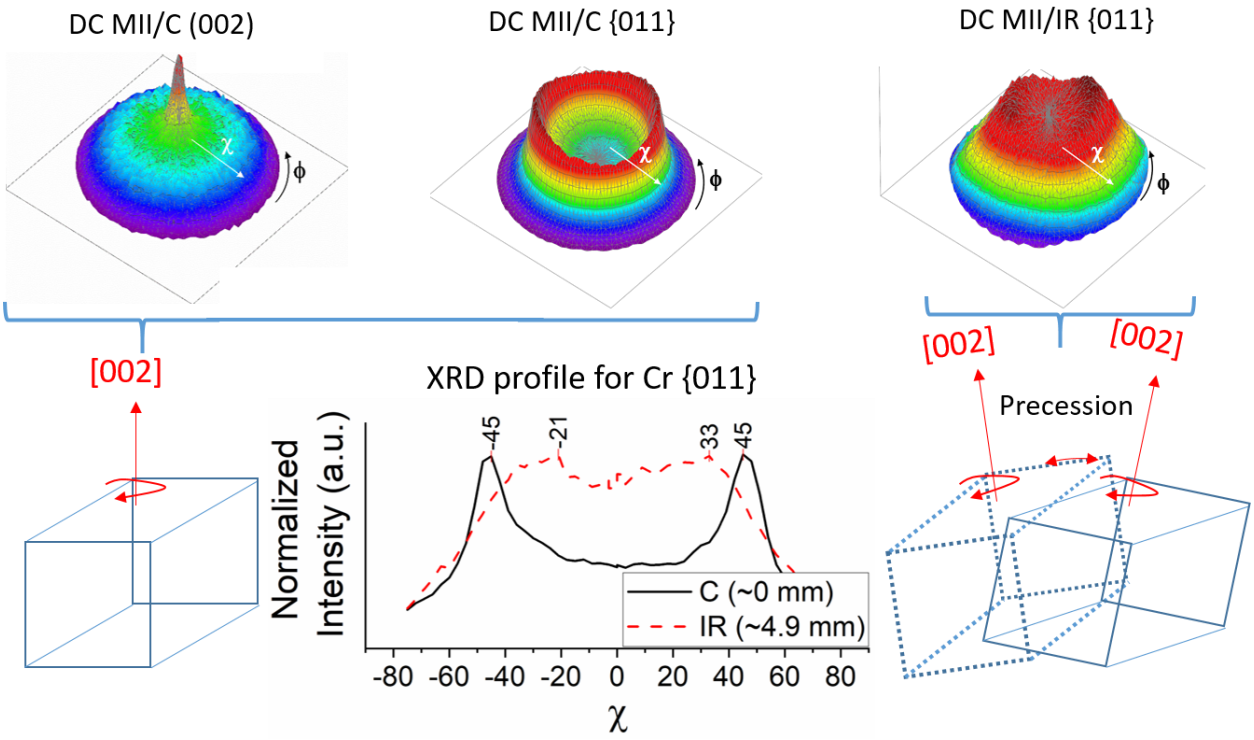

Figure 11. XRD texture analysis of the DC MII sample.

All the results presented for the DC samples give essential insights into the growth mechanism. It is known that when the energy of the sputtered species laying at the surface of the substrate is enough to overcome diffusion energy of the surface, the voids among columns start to fill, and defined crystals started to grow as observed in the IR position. However, only until the energy is high enough to promote atomic diffusion from grain to grain, the grains oriented in the higher crystal growth direction will overgrowth the grains with lower growth direction [34,46,80], leading to the structure in C position. Therefore, the lack of crystal texture, the presence of voids between the columnar grains, and the SEM and TEM images in Figure 9 and Figure 10 suggest low deposition species energy in the DC NM, DC MT, and the OR position of the DC MII. Furthermore, the density and the observed changes in texture from the C position towards the OR position

in DC MII indicate decreased species energy, demonstrated for the large voids and defects detected in the top-view and cross-sectional images.

3.5. Structural Morphology of HiPIMS Samples

The surface and cross-sectional SEM images presented in Figure 12 correspond to the HP samples. All three samples hold a columnar grain growth with three-fold symmetry pyramidal ends of about 26 nm average size. The cross-sectional images presented from Figure 12d through Figure 12f made it possible to compare the thicknesses and densification of the three samples. The sample HP MII was the thinnest sample, but it also showed a lower density of voids.

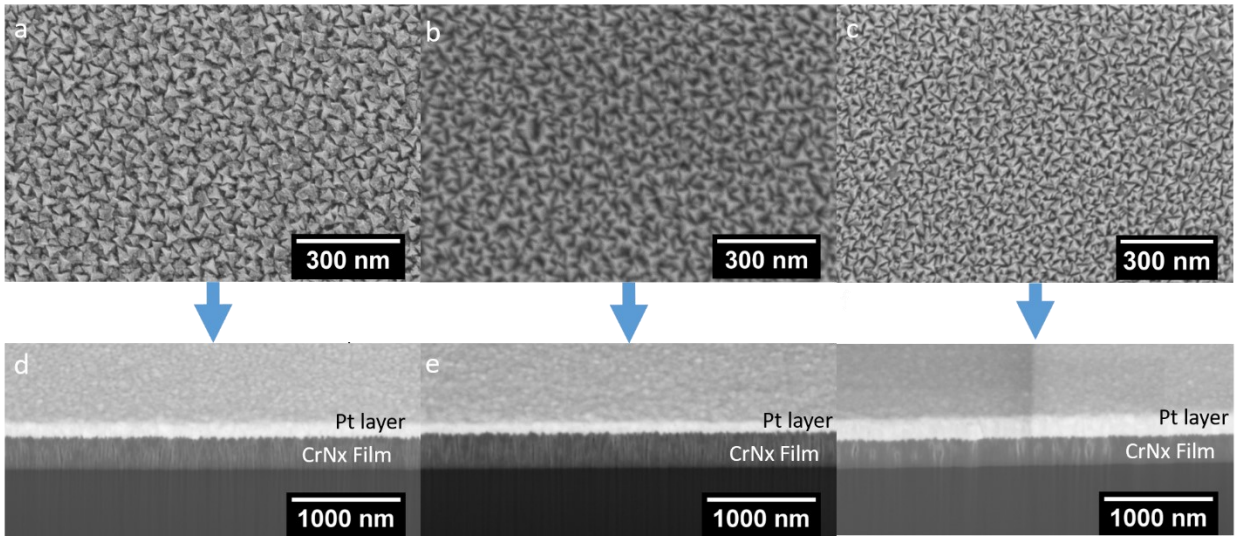

Figure 12. Surface and cross-section of the HP samples. a. surface of HP NM. b. surface of HP MT. c. surface of HP MII. d. cross-section of HP NM. e. cross-section of HP MT. f. cross-section of HPMII.

The crystal texture of the three HiPIMS samples has been evaluated by sweeping for the X-Ray intensity of chromium nitride (ICDD 00-011-0065) reflections (111), (200), and (220) in the χ and Ø angles. The whole set of (111) (200) and (220) pole figures can be found in supplementary data Figures from C4 through C6. The pole figures for the {111} reflections and analysis are presented in Figure 13. The main

peak at $\chi = 0$ indicates a strong crystal texture out-of-the-plane in the direction [111] for all three HiPIMS samples. The blue ring at high χ values (~70°) in all three pole figures indicate multiples grains rotate around the axis in the direction [111]. Figure 13d compares the FWHM for the $\chi = 0$ peak and polar tilting angle between the {111} family planes. The highest FWHM and the lowest angle between all the {111} reflections correspond for the HP MII sample.

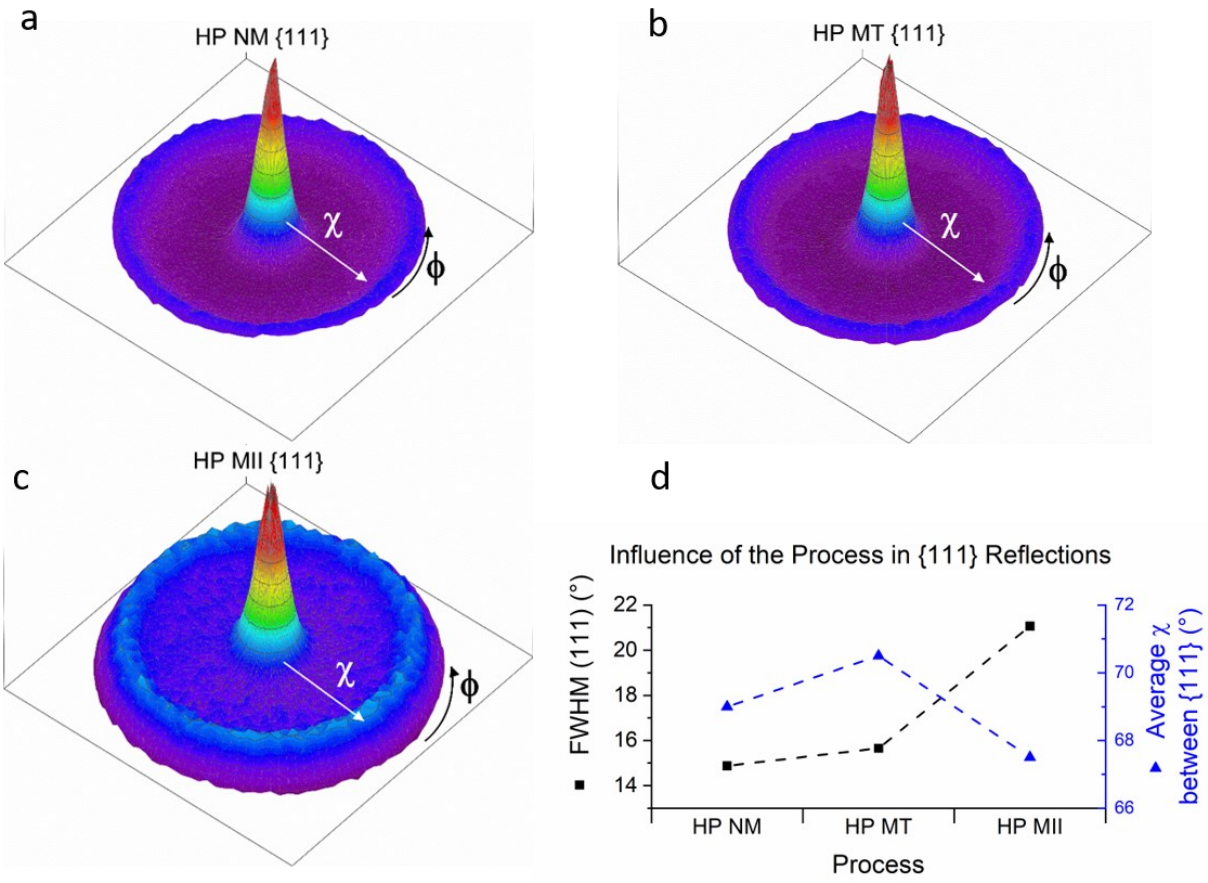

Figure 13. XRD texture measurements for the {111} reflections of CrN.

The analysis of the pole figures for CrN {111} in Figure 13 can give some qualitative pondering of the degree of texturizing of the sample's growth in the R-HiPIMS variants. The theoretical angle among the family {111} in a FCC cell is 70.53°, from (111) and (200) is 54.74, and from (111) to (220) is 35.26 °. The sharper the (111) peak in the out-of-plane direction $\chi = 0$ (lower FWHM) and the closer the angles

between reflections to the theoretic, the higher will be the film texture in the [111] direction. In this case, HP MII evidenced a higher deviation of such values[1]. The lower thickness of the films may explain the result. The grains with the fastest geometric growth will overgrowth the others, but this phenomenon will be set more with thickness evolution [46,80,81]. A low flux of sputtered material may explain the low thickness in the HP MII sample. Even though a flux of high-energy ions may cause etching on the films and reduce the film thickness, it would imply that planes with lower sputtering yield withstand better the bombarding with a concomitant texture in that direction. However, the three films have the same pyramidal topography that does not support the etching hypothesis. Besides, the crystal growth was in the direction [111], which theoretically has the highest sputtering yield [25,34,72,82–85].

The morphology in Figure 10, Figure 12, and texture in Figure 13 are congruent with a zone T structure presented by Mahieu's SZM [61]. These XRD texture analyses confirm the differences in film stoichiometries between the DC and HP samples discussed in section 3.2. Similarly, the different morphological features of grain size, shape, and structural defects between both processes can be linked to the film's stoichiometries and the species energy during the deposition processes [25,34,80]. Indeed, the addition of magnetic biasing nearby the substrate promotes reproducible and interesting results affecting the plasma species, the deposition rates, and modifying the structure of the deposited films when adequately combined with the classical parameter for both R-DCMS and R-HiPIMS processes.

4. Conclusions

The magnetic mirroring effect of the magnetic biasing configurations led to plasma confinement that boosted chromium species' ionization in R-DCMS and R-HiPIMS processes.

[1] It should be notice the uncertainty that introduces the step size of the χ and $\emptyset$ sweeps. Figure 1 presents the average values, but the closer measurements to 70.53^0 were done at $\chi = 69^0$ and $\chi = 72^0$.

The incorporation of nitrogen in the lattice of the chromium films changed through the combination of plasma generator and magnetic field configuration. The R-DCMS processes primarily formed chromium films with nitrogen in solid solution, whereas the R-HiPIMS processes were associated with chromium nitride. The HP MII configuration showed the highest atomic composition of nitrogen among all samples.

The fine plasma manipulation introduced by the magnetic biasing influenced the crystal growth, film structure, and thickness without modifying the traditional sputtering parameters such as pressure, gas mixture, target power, substrate temperature, electrical bias, or deposition time. The highest impact in both magnetic biasing options was for the MII configuration. The DC MII boosted the deposition rate selectively at the center of the magnetic field, offering the possibility of increase the thickness above three times of the conventional R-DCMS. However, the structure across the surface of DC MII samples varies from highly dense and texturized columns of Cr at the center to nanocrystalline growth with voids among columns at the edge of the magnet in the magnetic biasing. This focused increment of deposition rate may be used for patterning or fabrication of mems. In the HP MII counterpart, the deposition rate dropped due to the recycling cycle due to the high presence of chromium ions, but this sample also showed the highest incorporation of nitrogen. Since all samples were grown in similar deposition conditions, the changes of deposition rate, densification, and texture result from the magnetic biasing, either by the thermalization and ionization boost of the sputtered species or by the change in the deposition flux on the substrate's surface.

5. Acknowledgment

The authors gratefully acknowledge funding support from the NSF CAREER award # 2042982. The authors also acknowledge the support from the Biomagnetics Laboratory and the access to the Nanomaterials Core Characterization Facility at Virginia Commonwealth University.

6. References

[1] I. Adamovich, S.D. Baalrud, A. Bogaerts, P.J. Bruggeman, M. Cappelli, V. Colombo, U. Czarnetzki, U. Ebert, J.G. Eden, P. Favia, D.B. Graves, S. Hamaguchi, G. Hieftje, M. Hori, I.D. Kaganovich, U. Kortshagen, M.J. Kushner, N.J. Mason, S. Mazouffre, S.M. Thagard, H.R. Metelmann, A. Mizuno, E. Moreau, A.B. Murphy, B.A. Niemira, G.S. Oehrlein, Z.L. Petrovic, L.C. Pitchford, Y.K. Pu, S. Rauf, O. Sakai, S. Samukawa, S. Starikovskaia, J. Tennyson, K. Terashima, M.M. Turner, M.C.M. Van De Sanden, A. Vardelle, The 2017 Plasma Roadmap: Low temperature plasma science and technology, J. Phys. D. Appl. Phys. 50 (2017) 323001. https://doi.org/10.1088/1361-6463/aa76f5.

[2] K. Sarakinos, J. Alami, S. Konstantinidis, High power pulsed magnetron sputtering: A review on scientific and engineering state of the art, Surf. Coatings Technol. 204 (2010) 1661–1684. https://doi.org/10.1016/j.surfcoat.2009.11.013.

[3] P.J. Kelly, R.D. Arnell, Magnetron sputtering: A review of recent developments and applications, Vacuum. 56 (2000) 159–172. https://doi.org/10.1016/S0042-207X(99)00189-X.

[4] J.T. Gudmundsson, Physics and technology of magnetron sputtering discharges, Plasma Sources Sci. Technol. 29 (2020) 113001. https://doi.org/10.1088/1361-6595/abb7bd.

[5] B. Window, N. Savvides, Charged particle fluxes from planar magnetron sputtering sources, J. Vac. Sci. Technol. A. 4 (1986) 196–202. https://doi.org/10.1116/1.573470.

[6] D.L. Smith, Thin-Film Deposition: Principles and Practice, McGraw-Hill Education, 1995.

[7] V. Kouznetsov, K. Macák, J.M. Schneider, U. Helmersson, I. Petrov, A novel pulsed magnetron sputter technique utilizing very high target power densities, Surf. Coatings Technol. 122 (1999) 290–293. https://doi.org/10.1016/S0257-8972(99)00292-3.

[8] A. Anders, Tutorial: Reactive high power impulse magnetron sputtering (R-HiPIMS), J. Appl. Phys. 121 (2017) 171101. https://doi.org/10.1063/1.4978350.

[9] A. Anders, Deposition rates of high power impulse magnetron sputtering: Physics and economics, J. Vac. Sci. Technol. A Vacuum, Surfaces, Film. 28 (2010) 783–790. https://doi.org/10.1116/1.3299267.

[10] H. Hajihoseini, M. Čada, Z. Hubička, S. Ünaldi, M.A. Raadu, N. Brenning, J.T. Gudmundsson, D. Lundin, The Effect of Magnetic Field Strength and Geometry on the Deposition Rate and Ionized Flux Fraction in the HiPIMS Discharge, Plasma. 2 (2019) 201–221. https://doi.org/10.3390/plasma2020015.

[11] G. Greczynski, L. Hultman, Time and energy resolved ion mass spectroscopy studies of the ion flux during high power pulsed magnetron sputtering of Cr in Ar and Ar/N2 atmospheres, Vacuum. 84 (2010) 1159–1170. https://doi.org/10.1016/j.vacuum.2010.01.055.

[12] R.P.B. Viloan, D. Lundin, J. Keraudy, U. Helmersson, Tuning the stress in TiN films by regulating the doubly charged ion fraction in a reactive HiPIMS discharge, J. Appl. Phys. 127 (2020) 103302. https://doi.org/10.1063/1.5134003.

[13] N. Brenning, I. Axnäs, M.A. Raadu, D. Lundin, U. Helmerson, A bulk plasma model for dc and HiPIMS magnetrons, Plasma Sources Sci. Technol. 17 (2008). https://doi.org/10.1088/0963-0252/17/4/045009.

[14] L. Meng, H. Yu, J.R. Sporre, P. Raman, M.M. Szott, J.T. McLain, D.N. Ruzic, Direct measurement and modeling of the redirected ion flux in a high-powered pulsed-plasma magnetron, J. Vac. Sci. Technol. A. 33 (2015) 31301. https://doi.org/10.1116/1.4914174.

[15] M.L. Cedeño-Vente, G.C. Mondragón-Rodríguez, N. Camacho, A.E. Gómez-Ovalle, J.M. Gonzalez-Carmona, J.M. Alvarado-Orozco, D.G. Espinosa-Arbelaez, Tailoring the chemical composition and microstructure of CrxN deposited by HiPIMS through duty-cycle modifications, Surf. Coatings Technol. 422 (2021) 127502. https://doi.org/10.1016/J.SURFCOAT.2021.127502.

[16] Z. Wu, X. Tian, Z. Wang, C. Gong, S. Yang, C.M. Tan, P.K. Chu, Microstructure and mechanical properties of CrN films fabricated by high power pulsed magnetron discharge plasma immersion ion implantation and deposition, Appl. Surf. Sci. 258 (2011) 242–246. https://doi.org/10.1016/j.apsusc.2011.08.039.

[17] L. Zauner, P. Ertelthaler, T. Wojcik, H. Bolvardi, S. Kolozsvári, P.H. Mayrhofer, H. Riedl, Reactive HiPIMS deposition of Ti-Al-N: Influence of the deposition parameters on the cubic to hexagonal phase transition, Surf. Coatings Technol. 382 (2020) 125007. https://doi.org/10.1016/j.surfcoat.2019.125007.

[18] V. Sittinger, O. Lenck, M. Vergöhl, B. Szyszka, G. Bräuer, Applications of HIPIMS metal oxides, Thin Solid Films. 548 (2013) 18–26. https://doi.org/10.1016/j.tsf.2013.08.087.

[19] T. Hänninen, S. Schmidt, J. Jensen, L. Hultman, H. Högberg, Silicon oxynitride films deposited by reactive high power impulse magnetron sputtering using nitrous oxide as a single-source precursor, J. Vac. Sci. Technol. A Vacuum, Surfaces, Film. 33 (2015) 05E121. https://doi.org/10.1116/1.4927493.

[20] M. Lattemann, U. Helmersson, J.E. Greene, Fully dense, non-faceted 111-textured high power impulse magnetron sputtering TiN films grown in the absence of substrate heating and bias, Thin Solid Films. 518 (2010) 5978–5980. https://doi.org/10.1016/j.tsf.2010.05.064.

[21] F. Magnus, A.S. Ingason, S. Olafsson, J.T. Gudmundsson, Nucleation and resistivity of ultrathin TiN films grown by high-power impulse magnetron sputtering, IEEE Electron Device Lett. 33 (2012) 1045–1047. https://doi.org/10.1109/LED.2012.2196018.

[22] K. Sarakinos, D. Magnfält, V. Elofsson, B. Lü, Atomistic view on thin film nucleation and growth by using highly ionized and pulsed vapour fluxes, Surf. Coatings Technol. 257 (2014) 326–332. https://doi.org/10.1016/j.surfcoat.2014.04.015.

[23] Y.P. Purandare, A.P. Ehiasarian, P.E. Hovsepian, Deposition of nanoscale multilayer CrN/NbN physical vapor deposition coatings by high power impulse magnetron sputtering, J. Vac. Sci. Technol. A Vacuum, Surfaces, Film. 26 (2008) 288–296. https://doi.org/10.1116/1.2839855.

[24] R. Hippler, Z. Hubicka, M. Cada, P. Ksirova, H. Wulff, C.A. Helm, V. Stranak, Angular dependence of plasma parameters and film properties during high power impulse magnetron sputtering for deposition of Ti and TiO2 layers, J. Appl. Phys. 121 (2017) 171906. https://doi.org/10.1063/1.4977823.

[25] F. Ferreira, J.C. Oliveira, A. Cavaleiro, CrN thin films deposited by HiPIMS in DOMS mode, Surf. Coatings Technol. 291 (2016) 365–375. https://doi.org/10.1016/j.surfcoat.2016.02.064.

[26] H. Zhang, J.-S. Cherng, Q. Chen, Recent progress on high power impulse magnetron sputtering (HiPIMS): The challenges and applications in fabricating VO2 thin film, AIP Adv. 9 (2019) 35242.

https://doi.org/10.1063/1.5084031.

[27] A. Anders, Discharge physics of high power impulse magnetron sputtering, Surf. Coatings Technol. 205 (2011) S1–S9. https://doi.org/10.1016/j.surfcoat.2011.03.081.

[28] O. Antonin, V. Tiron, C. Costin, G. Popa, T.M. Minea, On the HiPIMS benefits of multi-pulse operating mode, J. Phys. D. Appl. Phys. 48 (2015) 015202. https://doi.org/10.1088/0022-3727/48/1/015202.

[29] S.D. Ekpe, F.J. Jimenez, D.J. Field, M.J. Davis, S.K. Dew, Effect of magnetic field strength on deposition rate and energy flux in a dc magnetron sputtering system, J. Vac. Sci. Technol. A. 27 (2009) 1275–1280. https://doi.org/10.1116/1.3222874.

[30] V. Tiron, I.-L. Velicu, I. Mihăilă, G. Popa, Deposition rate enhancement in HiPIMS through the control of magnetic field and pulse configuration, Surf. Coatings Technol. 337 (2018) 484–491. https://doi.org/10.1016/j.surfcoat.2018.01.065.

[31] A.P. Ehiasarian, W.-D. Münz, L. Hultman, U. Helmersson, I. Petrov, High power pulsed magnetron sputtered CrNx films, Surf. Coatings Technol. 163–164 (2003) 267–272. https://doi.org/10.1016/S0257-8972(02)00479-6.

[32] G. Greczynski, J. Lu, J. Jensen, S. Bolz, W. Kölker, C. Schiffers, O. Lemmer, J.E. Greene, L. Hultman, A review of metal-ion-flux-controlled growth of metastable TiAlN by HIPIMS/DCMS co-sputtering, Surf. Coatings Technol. 257 (2014) 15–25. https://doi.org/10.1016/j.surfcoat.2014.01.055.

[33] A.P. Ehiasarian, A. Vetushka, Y.A. Gonzalvo, G. Sáfrán, L. Székely, P.B. Barna, Influence of high power impulse magnetron sputtering plasma ionization on the microstructure of TiN thin films, J. Appl. Phys. 109 (2011) 104314. https://doi.org/10.1063/1.3579443.

[34] A. Anders, A structure zone diagram including plasma-based deposition and ion etching, Thin Solid Films. 518 (2010) 4087–4090. https://doi.org/10.1016/j.tsf.2009.10.145.

[35] M. Trant, M. Fischer, K. Thorwarth, S. Gauter, J. Patscheider, H.J. Hug, Tunable ion flux density and its impact on AlN thin films deposited in a confocal DC magnetron sputtering system, Surf. Coatings Technol. 348 (2018) 159–167. https://doi.org/10.1016/j.surfcoat.2018.04.091.

[36] I.-L. Velicu, V. Tiron, C. Porosnicu, I. Burducea, N. Lupu, G. Stoian, G. Popa, D. Munteanu, Enhanced properties of tungsten thin films deposited with a novel HiPIMS approach, Appl. Surf. Sci. 424 (2017) 397–406. https://doi.org/10.1016/j.apsusc.2017.01.067.

[37] S. Sevvana, S. Chennadi, R.K. Lakkaraju, J. Li, D.M. Mihut, S.L. Rohde, Rate enhancement in high power pulsed magnetron sputtering growth using secondary discharge confinement, in: Proceedings, Annu. Tech. Conf. - Soc. Vac. Coaters, Denver, CO, 2005: pp. 720–725.

[38] J. Bohlmark, M. Östbye, M. Lattemann, H. Ljungcrantz, T. Rosell, U. Helmersson, Guiding the deposition flux in an ionized magnetron discharge, Thin Solid Films. 515 (2006) 1928–1931. https://doi.org/10.1016/j.tsf.2006.07.183.

[39] J. Keraudy, R.P.B. Viloan, M.A. Raadu, N. Brenning, D. Lundin, U. Helmersson, Bipolar HiPIMS for tailoring ion energies in thin film deposition, Surf. Coatings Technol. 359 (2019) 433–437. https://doi.org/10.1016/j.surfcoat.2018.12.090.

[40] J. Vlček, P. Kudláček, K. Burcalová, J. Musil, High-power pulsed sputtering using a magnetron with

enhanced plasma confinement, J. Vac. Sci. Technol. A. 25 (2007) 42–47. https://doi.org/10.1116/1.2388954.

[41] J. Alami, Z. Maric, H. Busch, F. Klein, U. Grabowy, M. Kopnarski, Enhanced ionization sputtering: A concept for superior industrial coatings, Surf. Coatings Technol. 255 (2014) 43–51. https://doi.org/10.1016/j.surfcoat.2013.11.040.

[42] A. Hecimovic, A.P. Ehiasarian, Time evolution of ion energies in HIPIMS of chromium plasma discharge, J. Phys. D. Appl. Phys. 42 (2009) 135209. https://doi.org/10.1088/0022-3727/42/13/135209.

[43] S.J. Strickler, The identification of molecular spectra (Pearse, R. W. B.; Gaydon, A. G.), J. Chem. Educ. 41 (1964) A398. https://doi.org/10.1021/ed041pa398.

[44] Z. Navrátil, D. Trunec, R. Šmíd, L. Lazar, A software for optical emission spectroscopy-problem formulation and application to plasma diagnostics, Czechoslov. J. Phys. 56 (2006) B944–B951. https://doi.org/10.1007/s10582-006-0308-y.

[45] P. Raman, Magnetic Field Optimization for High Power Impulse Magnetron Sputtering, Doctoral dissertation, University of Illinois, 2016.

[46] I. Petrov, P.B. Barna, L. Hultman, J.E. Greene, Microstructural evolution during film growth, J. Vac. Sci. Technol. A. 21 (2003) S117–S128. https://doi.org/10.1116/1.1601610.

[47] M. Zeuner, J. Meichsner, Ion kinetics in collisional rf-glow discharge sheaths, Vacuum. 46 (1995) 151–157. https://doi.org/10.1016/0042-207X(94)E0030-3.

[48] I. Petrov, A. Myers, J.E. Greene, J.R. Abelson, Mass and energy resolved detection of ions and neutral sputtered species incident at the substrate during reactive magnetron sputtering of Ti in mixed Ar+N 2 mixtures, J. Vac. Sci. Technol. A Vacuum, Surfaces, Film. 12 (1994) 2846–2854. https://doi.org/10.1116/1.578955.

[49] B. Wu, I. Haehnlein, I. Shchelkanov, J. McLain, D. Patel, J. Uhlig, B. Jurczyk, Y. Leng, D.N. Ruzic, Cu films prepared by bipolar pulsed high power impulse magnetron sputtering, Vacuum. 150 (2018) 216–221. https://doi.org/10.1016/j.vacuum.2018.01.011.

[50] Y.J. Kim, Y.S. Choi, K.S. Shin, S.H. Cho, I.S. Choi, J.G. Han, High deposition rate microcrystalline silicon films prepared by magnetic mirror assisted RF-PECVD, in: Curr. Appl. Phys., North-Holland, 2010: pp. S354–S356. https://doi.org/10.1016/j.cap.2010.02.010.

[51] C. Strobel, G. Gantefoer, A. Bodi, P. Hemberger, Gridless electron trap for a high-duty cycle magnetic bottle time-of-flight spectrometer, J. Electron Spectros. Relat. Phenomena. 239 (2020) 146900. https://doi.org/10.1016/j.elspec.2019.146900.

[52] D. Lundin, The HiPIMS Process, Doctoral dissertation, Linköping University, 2010.

[53] D.J. Christie, Target material pathways model for high power pulsed magnetron sputteringa), J. Vac. Sci. Technol. A Vacuum, Surfaces, Film. 23 (2005) 330. https://doi.org/10.1116/1.1865133.

[54] D. Depla, R. De Gryse, Target poisoning during reactive magnetron sputtering: Part I: the influence of ion implantation, Surf. Coatings Technol. 183 (2004) 184–189. https://doi.org/10.1016/j.surfcoat.2003.10.006.

[55] R. Ganesan, B.J. Murdoch, B. Treverrow, A.E. Ross, I.S. Falconer, A. Kondyurin, D.G. McCulloch,

J.G. Partridge, D.R. McKenzie, M.M.M. Bilek, The role of pulse length in target poisoning during reactive HiPIMS: application to amorphous HfO2, Plasma Sources Sci. Technol. 24 (2015) 35015. https://doi.org/10.1088/0963-0252/24/3/035015.

[56] H. Hajihoseini, M. Čada, Z. Hubička, S. Ünaldi, M.A. Raadu, N. Brenning, J.T. Gudmundsson, D. Lundin, Sideways deposition rate and ionized flux fraction in dc and high power impulse magnetron sputtering, J. Vac. Sci. Technol. A Vacuum, Surfaces, Film. 38 (2020) 033009. https://doi.org/10.1116/1.5145292.

[57] J. Held, A. von Keudell, Pattern Formation in High Power Impulse Magnetron Sputtering (HiPIMS) Plasmas, Plasma Chem. Plasma Process. 40 (2020) 643–660. https://doi.org/10.1007/s11090-019-10052-3.

[58] R.V.E. Lovelace, C. Mehanian, T.J. Tommila, D.M. Lee, Magnetic confinement of a neutral gas, Nat. 1985 3186041. 318 (1985) 30–36. https://doi.org/10.1038/318030a0.

[59] G. Reinaudi, T. Lahaye, A. Couvert, Z. Wang, D. Guéry-Odelin, Evaporation of an atomic beam on a material surface, Phys. Rev. A - At. Mol. Opt. Phys. 73 (2006) 14–16. https://doi.org/10.1103/PhysRevA.73.035402.

[60] E.A. Hinds, I.G. Hughes, Magnetic atom optics: Mirrors, guides, traps, and chips for atoms, J. Phys. D. Appl. Phys. 32 (1999). https://doi.org/10.1088/0022-3727/32/18/201.

[61] V.I. Balykin, V.G. Minogin, V.S. Letokhov, Electromagnetic trapping of cold atoms, Reports Prog. Phys. 63 (2000) 1429. https://doi.org/10.1088/0034-4885/63/9/202.

[62] D. Briggs, X-ray photoelectron spectroscopy (XPS), Perkin-Elmer Corporation, Eden prairie, 2005. https://doi.org/10.1002/0470014229.ch22.

[63] I. Milošev, H.-H. Strehblow, B. Navinšek, P. Panjan, Chromium Nitride by XPS, Surf. Sci. Spectra. 5 (1998) 138–144. https://doi.org/10.1116/1.1247871.

[64] Y. Li, H. Xu, F. Zhu, L. Wang, Low temperature anodic nitriding of AISI 304 austenitic stainless steel, Mater. Lett. 128 (2014) 231–234. https://doi.org/10.1016/j.matlet.2014.04.121.

[65] J.P. Riviere, M. Cahoreau, P. Meheust, Chemical bonding of nitrogen in low energy high flux implanted austenitic stainless steel, J. Appl. Phys. 91 (2002) 6361–6366. https://doi.org/10.1063/1.1469691.

[66] M.K. Lei, X.M. Zhu, Chemical state of nitrogen in a high nitrogen face-centered-cubic phase formed on plasma source ion nitrided austenitic stainless steel, J. Vac. Sci. Technol. A Vacuum, Surfaces, Film. 22 (2004) 2067–2070. https://doi.org/10.1116/1.1786305.

[67] W. Liang, X. Xiaolei, X. Jiujun, S. Yaqin, Characteristics of low pressure plasma arc source ion nitrided layer on austenitic stainless steel at low temperature, Thin Solid Films. 391 (2001) 11–16. https://doi.org/10.1016/S0040-6090(01)00969-5.

[68] K. Sykam, K.K.R. Meka, S. Donempudi, Intumescent Phosphorus and Triazole-Based Flame-Retardant Polyurethane Foams from Castor Oil, ACS Omega. 4 (2019) 1086–1094. https://doi.org/10.1021/acsomega.8b02968.

[69] Z. Ahmad, M.A. Najeeb, R.A. Shakoor, A. Alashraf, S.A. Al-Muhtaseb, A. Soliman, M.K. Nazeeruddin, Instability in CH3NH3PbI3 perovskite solar cells due to elemental migration and

chemical composition changes, Sci. Rep. 7 (2017) 15406. https://doi.org/10.1038/s41598-017-15841-4.

[70] J.B. Nelson, D.P. Riley, An experimental investigation of extrapolation methods in the derivation of accurate unit-cell dimensions of crystals, Proc. Phys. Soc. 57 (1945) 160–177. https://doi.org/10.1088/0959-5309/57/3/302.

[71] R. Sathyamoorthy, J. Dheepa, Structural characterization of thermally evaporated Bi2Te3 thin films, J. Phys. Chem. Solids. 68 (2007) 111–117. https://doi.org/10.1016/j.jpcs.2006.09.014.

[72] G. Greczynski, J. Jensen, L. Hultman, CrNx films prepared by DC magnetron sputtering and high-power pulsed magnetron sputtering: A comparative study, in: IEEE Trans. Plasma Sci., 2010: pp. 3046–3056. https://doi.org/10.1109/TPS.2010.2071885.

[73] D. Kim, K. Lee, Y.S. Yoon, Effect of CrN barrier on fuel-clad chemical interaction, Nucl. Eng. Technol. 50 (2018) 724–730. https://doi.org/10.1016/j.net.2018.02.008.

[74] J. Lin, W.D. Sproul, J.J. Moore, S. Lee, S. Myers, High rate deposition of thick CrN and Cr2N coatings using modulated pulse power (MPP) magnetron sputtering, Surf. Coatings Technol. 205 (2011) 3226–3234. https://doi.org/10.1016/j.surfcoat.2010.11.039.

[75] Z.B. Qi, B. Liu, Z.T. Wu, F.P. Zhu, Z.C. Wang, C.H. Wu, A comparative study of the oxidation behavior of Cr2N and CrN coatings, Thin Solid Films. 544 (2013) 515–520. https://doi.org/10.1016/j.tsf.2013.01.031.

[76] J. Alami, K. Sarakinos, F. Uslu, M. Wuttig, On the relationship between the peak target current and the morphology of chromium nitride thin films deposited by reactive high power pulsed magnetron sputtering, J. Phys. D. Appl. Phys. 42 (2008) 15304. https://doi.org/10.1088/0022-3727/42/1/015304.

[77] J.D. Weinstein, R. deCarvalho, J. Kim, D. Patterson, B. Friedrich, J.M. Doyle, Magnetic trapping of atomic chromium, Phys. Rev. A - At. Mol. Opt. Phys. 57 (1998) R3173–R3175. https://doi.org/10.1103/PhysRevA.57.R3173.

[78] A. Griesmaier, J. Werner, S. Hensler, J. Stuhler, T. Pfau, Bose-Einstein condensation of chromium, Phys. Rev. Lett. 94 (2005) 160401. https://doi.org/10.1103/PhysRevLett.94.160401.

[79] R. Chicireanu, A. Pouderous, R. Barbé, B. Laburthe-Tolra, E. Maréchal, L. Vernac, J.C. Keller, O. Gorceix, Simultaneous magneto-optical trapping of bosonic and fermionic chromium atoms, Phys. Rev. A - At. Mol. Opt. Phys. 73 (2006) 053406. https://doi.org/10.1103/PhysRevA.73.053406.

[80] S. Mahieu, P. Ghekiere, D. Depla, R. De Gryse, Biaxial alignment in sputter deposited thin films, Thin Solid Films. 515 (2006) 1229–1249. https://doi.org/10.1016/j.tsf.2006.06.027.

[81] H. Era, Y. Ide, A. Nino, K. Kishitake, TEM study on chromium nitride coatings deposited by reactive sputter method, Surf. Coatings Technol. 194 (2005) 265–270. https://doi.org/10.1016/j.surfcoat.2004.05.022.

[82] R. Messier, A.P. Giri, R.A. Roy, Revised structure zone model for thin film physical structure, J. Vac. Sci. Technol. A. 2 (1984) 500–503. https://doi.org/10.1116/1.572604.

[83] T. Karabacak, Thin-film growth dynamics with shadowing and re-emission effects, J.

Nanophotonics. 5 (2011) 52501. https://doi.org/10.1117/1.3543822.

[84] L. Hultman, W. -D. Münz, J. Musil, S. Kadlec, I. Petrov, J.E. Greene, Low-energy (~100 eV) ion irradiation during growth of TiN deposited by reactive magnetron sputtering: Effects of ion flux on film microstructure, J. Vac. Sci. Technol. A. 9 (1991) 434–438. https://doi.org/10.1116/1.577428.

[85] J.P. Zhao, X. Wang, Z.Y. Chen, S.Q. Yang, T.S. Shi, X.H. Liu, Overall energy model for preferred growth of TiN films during filtered arc deposition, J. Phys. D. Appl. Phys. 30 (1997) 5–12. https://doi.org/10.1088/0022-3727/30/1/002.